This is an accepted version of the paper ID24 “Modeling the effect of temperature on relative humidity sensing” by Maria Vesna Nikolic and Sreten Mastilovic, presented at the 46th International Spring Seminar on Electronics Technology (ISSE), May 10-14, Timisoara, Romania and the full version of the paper was published in the Proceedings of 2023 46th International Spring Seminar on Electronics Technology (ISSE) by IEEE https://ieeexplore.ieee.org/xpl/conhome/10168303/proceeding and the link to the paper is https://ieeexplore.ieee.org/document/10168374 and DOI:10.1109/ISSE57496.2023.10168374

Modeling the effect of temperature on relative humidity sensing

Maria Vesna Nikolic, Sreten Mastilovic
University of Belgrade-Institute for Multidisciplinary Research, Belgrade, Serbia
mariavesna@imsi.rs

***Abstract*—In this work we have established a mathematical function to model the influence of the ambient temperature, relative humidity and frequency on the change of impedance. The proposed empirical description is a combination of the power function (modeling the temperature effect) and a reverse-sigmoid function inspired by the three-parameter Weibull cumulative distribution function (modeling the relative humidity and frequency effects). This empirical model was validated by using our iron manganite ($FeMnO_3$) thick film measurement data. The reduction of impedance of thick film samples with change in relative humidity in the range 30-90% was measured in a temperature and climatic chamber in the frequency range 42 Hz – 1 MHz at three ambient/working temperatures (25, 50 and 75 °C). The obtained experimental data was successfully fitted using the specially tailored empirical model. Application of this model enables prediction of the iron manganite sensor performance for different temperatures both within the confines of the analyzed temperature range (interpolation) and outside of it (extrapolation). Future development will include applying this model to analyzing the temperature influence on relative humidity sensing for other metal oxide sensing materials that have shown a similar dependence and in a wider ambient temperature range.**

Keywords—Modeling, Relative Humidity Sensing, Temperature, Frequency, Weibull model.

I. INTRODUCTION

Accurate and reliable monitoring of the change in humidity and moisture in diverse environments is an essential component of human health and safety, agricultural processes, weather forecasting and many industrial applications that include electronics, and food manufacturing processes [1]. Recent research has focused on flexible humidity sensor systems tracing the way towards more widespread application of portable and wearable electronics [2]. Humidity monitoring is commonly achieved using humidity sensors that measure the change in relative humidity (RH). Different materials, such as semiconducting metal oxides, polymers or composite/hybrid materials have been used as the sensing material in a relative humidity sensor [3, 4]. The humidity sensing mechanism is founded on the change in electrical properties (for resistance, impedance and capacitance) of the humidity sensing material surface when absorbing and desorbing water molecules [1].

Impedance-based sensors using semiconducting metal oxides and perovskites have been widely researched and commercially applied as RH sensing materials [5]. They are low cost materials that can be applied in small sized sensors commonly produced as thick or thin films on interdigitated electrodes on alumina or flexible substrates [3, 6, 7]. When investigating a semiconducting material for RH sensing one of the parameters that needs to be selected is the operating/working frequency. Research of the change in impedance with frequency different semiconducting metal oxides has shown that the impedance decreases as the frequency increases due to relaxation processes [8]. Lower frequency values, such as 100 Hz are often selected as the operating frequency, as the sensor sensitivity is higher, for instance ZrO_2 [6] or $FeMnO_3$ [9]. However, as output linearity also needs to be considered when selecting the operating frequency, as shown by Wu et al. [7], who chose 900 Hz for their impedance sensor, it is necessary to investigate the dependence of impedance on frequency for RH sensing.

The ambient temperature also has an influence on the performance of impedance sensors, as the impedance decreases with temperature due to increase in the sensing material conductance and decrease in relaxation time [8]. In the case of RH monitoring at a higher ambient temperature the impedance is lower due to increase in carriers in the sensing material and increased amount of ions of the adsorbed water molecules [6]. Commercial, practical application of RH impedance sensors can require some type of temperature compensation [7], thus, prediction of the sensor performance at different temperatures is one step towards achieving this. In this work we have developed an empirical model based on a combination of the power function and the Weibull cumulative distribution function and applied it to describe the measured change in impedance with temperature, frequency, and relative humidity of iron manganite ($FeMnO_3$) thick films. We have predicted the iron manganite humidity sensor performance both within the confines of the analyzed temperature range (25–75 °C) and outside it.

II. MATERIALS AND METHODS

A. *Thick film $FeMnO_3$ sensor*

Recent research has focused on the possible application of iron manganite ($FeMnO_3$), a mixed metal oxide for humidity sensing [9, 10]. The sensor was designed as a thick film screen printed on alumina substrate with interdigitated PdAg electrodes (8 mm width, 10 mm length, 0.3 mm electrode spacing and nine fingers), resulting in a 55 μm thick porous structure, as shown in Fig. 1. Detailed structural, morphological and textural properties of this sensing thick film were given in detail in [9], confirming the formation of pure phase iron manganite ($FeMnO_3$).

The sensing surface was composed of $FeMnO_3$ particles (495 nm on average) and a stable pore system (mostly

Ministry for Science, Technological Development and Innovations of the Republic of Serbia, contract number 451-03-47/2023-1/200053.

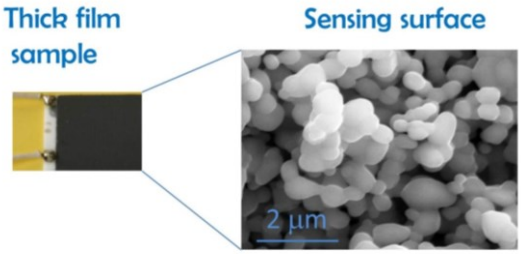

Fig. 1 Iron manganite ($FeMnO_3$) thick film sample image (left) and scanning electron image of sensing surface (right), magnification 30000×.

macropores 493 nm on average, but the pore system consisted of a wide distribution of pores) enabling good interaction with water molecules, as revealed in the micrograph in Fig. 1 recorded on a Tescan (VEGA TS 5130MM) scanning electron microscope, and magnification of 30000×. Relative humidity (RH) dependent impedance sensing was monitored in a humidity and temperature climatic chamber at room temperature (25 °C). The frequency of 100 Hz was selected as the operating frequency, as it provided a noticeable decrease in impedance (≈ 15.4 times), response and recovery in several seconds and a low hysteresis of 2.8% [9].

Measurement of the change of impedance ($Z = R+jX$, $|Z| = (R^2+X^2)^{1/2}$) of $FeMnO_3$ thick films with change in the RH in the frequency range $\nu \in$ [42 Hz, 1 MHz] at three working/ambient temperatures (25, 50 and 75 °C) was conducted in a humidity and temperature climatic chamber (JEIO TECH TH-KE-025) as described in detail in [10]. The selected frequency range was the maximum measuring range of the LCR analyzer (HIOKI 3532) used and included the 100 Hz – 1 KHz range where the change in impedance is the highest and where the operating frequency of impedance humidity sensors based on semiconducting materials is usually selected. We noted a reduction of the measured impedance with increase in frequency, RH and temperature [10], as shown in the example in Fig. 2.

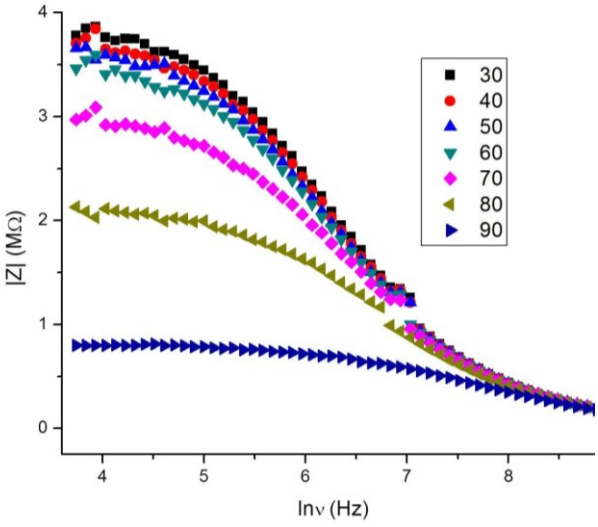

Fig. 2 Change of impedance (|Z|) with frequency (ν) in the relative humidity (RH) range 30-90% and ambient temperature of 50 °C

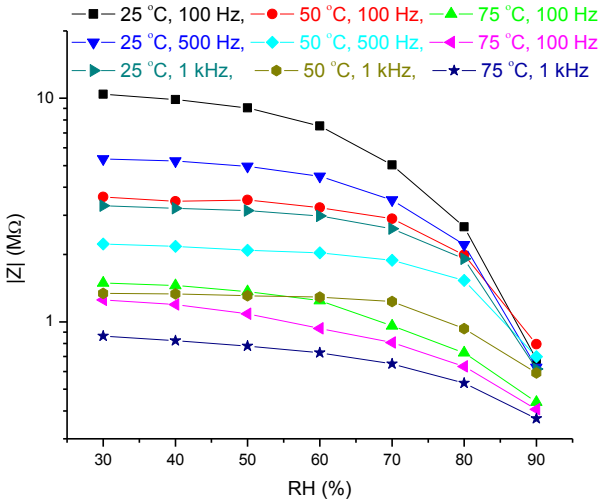

Fig. 3 Change of $FeMnO_3$ thick film impedance with relative humidity (RH), at temperatures (T) of 25, 50 and 75 °C, and frequencies (ν) of 100 Hz, 500 Hz and 1 kHz.

As the temperature increased the overall impedance was lower and so was the magnitude of the impedance decrease with increase in RH, as shown in Fig. 3.

B. Weibull modeling of physical phenomena

The Weibull model is applied often in the physical phenomena modeling including the weakest-link statistics and the reliability modeling [11, 12]. For example, Yu et al. [13] applied the Weibull model to define a method for improving the efficiency of the process of hot air drying of biological products by controlling the relative humidity. They determined that the shape parameter (β) in the Weibull model can be linked to the mass transfer rate determined at the start of the drying process. The Weibull distribution is also commonly applied to model wind speed data [14]. The Weibull model has also been applied to the analysis of such diverse phenomena as the combined effect of temperature and water activity on thermal resistance of bacteria [15] or the fracture toughness characterization of ferritic steels in ductile-to-brittle transition temperature region [16].

In the present study, the empirical description:

$$|Z| = |Z_0|_R \exp\left\{-\left[\frac{\ln \bar{\nu}}{\eta}\right]^{\beta} - \left[\frac{\overline{RH}-1}{\chi}\right]^{\kappa}\right\} \bar{T}^{-\tau} \qquad (1)$$

is custom-made with the objective to enable prediction of the impedance |Z| as a function of RH ($\overline{RH} = RH/RH_R$), frequency ($\bar{\nu} = \nu/\nu_R$), and ambient temperature ($\bar{T} = T/T_R$); (T [K]). The abovementioned parameters with subscript R mark the reference quantities ($RH_R = 30\%$, and $|Z_0|_R = 11.\,\text{M}\Omega$ in correlation with $T_R = 298$ K) used for normalization.[1] The Weibull parameters of scale (η, χ) and shape (β, κ) and the temperature exponent (τ) are determined by fitting the experimental data available in the recent article [10].

[1] Notably, the minimum measuring frequency of our LCR analyzer defines the default reference frequency $\nu_R = 42$ Hz that can be increased in the case of delayed impedance decrease, which is characteristic of the high RH levels (e.g., 80%, 90%) at elevated temperatures (Fig. 2).

III. WEIBULL MODEL OF $|Z|$ (ν, RH, T)

The novel model (1) captures reasonably well the qualitative impedance change, as shown in Fig. 4. The surface plots in Fig. 4 illustrate the general trends of the impedance change with temperature, RH, and frequency.

Estimation of the Weibull parameters of scale, shape and temperature exponent is discussed in the following sections.

A. Temperature sensitivity

The proposed empirical model (1) accounts for the temperature sensitivity of the impedance using the power law

$$|Z_0| = |Z_0|_R \cdot (T/T_R)^{-\tau} \tag{2}$$

where the reference values: $|Z_0|_R = 11.$ MΩ and $T_R = 298$ K correspond to $RH_R = 30\%$ and $\nu_R = 42$ Hz. The functional dependence (2) captures the reduction of the impedance upper-shelf value with the temperature increase. Our experimental results reveal the following data pairs: (T [K], Z_0 [MΩ]) = {(298, 11.07), (323, 3.78), (348, 1.52)}, which are, in the normalized form, represented by square symbols in the logarithmic plot in Fig. 5. Application of logarithm on both sides of Eq. (2) results in the expression:

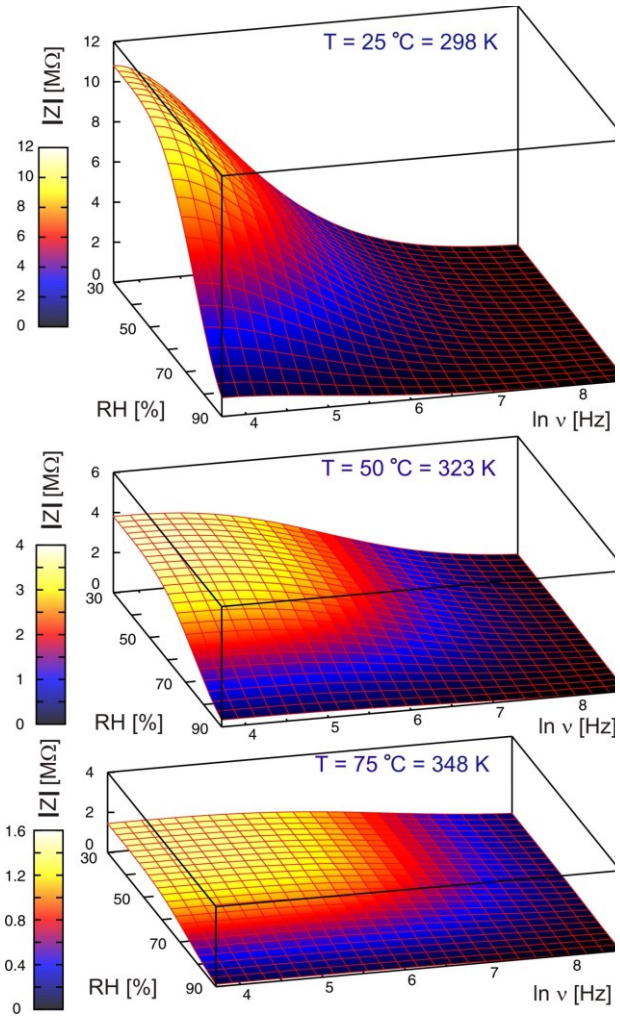

Fig 4 Mathematical representation of the impedance surface $|Z|$ in the RH–ln ν (frequency) space at temperatures T = 25, 50 and 75 °C

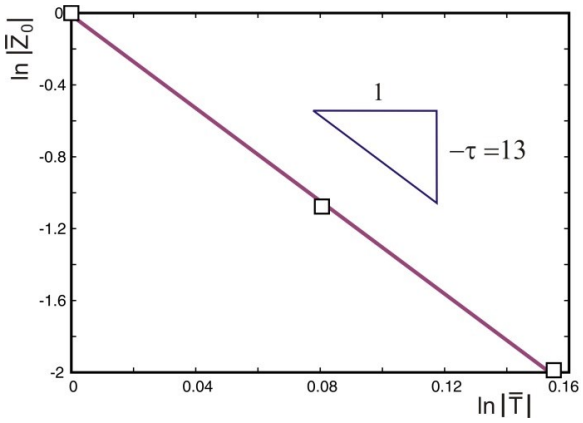

Fig. 5 Estimation of the power exponent τ, governing the temperature sensitivity of the impedance, using a logarithmic plot.

$$\ln\left(|Z_0|/|Z_0|_R\right) = -\tau \cdot \ln\left(T/T_R\right) \tag{3}$$

that is convenient for estimation of the power-law exponent τ since it represents the slope of the linear fit in Fig. 5.

Therefore, the exponent of the power law (2) is estimated based on experimental evidence to be $\tau \approx 13.0$ with three-significant digits accuracy. Notably, this is just an initial estimate, the final value is determined based on fitting of the experimental data depicting the change of impedance with frequency (e.g., Fig. 1); see Table II.

B. RH sensitivity

The empirical model (1) accounts for the RH sensitivity of the impedance using the Weibull-type function:

$$y = y_0 \cdot \exp\left\{-\left(\frac{x}{A}\right)^B\right\} \tag{4}$$

In the case of RH sensitivity, the dependent variable is impedance ($y = |Z|$), the independent variable is the translated normalized RH ($x = RH/30 - 1$), while the corresponding Weibull parameters of scale and shape are indicated in Eq. (1) as $A = \chi$ and $B = \kappa$, respectively. Two consecutive applications of logarithm on both sides of Eq. (4) result in the following expression:

$$\ln\left(-\ln\left(y/y_0\right)\right) = B \cdot \left(\ln x - \ln A\right) \tag{5}$$

that is convenient for estimation of the Weibull parameters for known experimental data points (x, y) (Fig. 3).

It should not be overlooked that the plots in Fig. 3, illustrating the change of $FeMnO_3$ thick film impedance with RH, clearly indicate that a rapid impedance reduction takes place as soon as a certain RH threshold is reached and this is in accordance with the humidity sensing mechanism of chemisorption and physisorption [9]. The phenomenology seems to indicate a percolation-type mechanism. According to Fig. 3, the temperature increase reduces this threshold value, which is in accordance with our intuitive expectation.

As an example, Fig. 6 illustrates the Weibull plot corresponding to Eq. (5), obtained for the experimental data for frequency 42 Hz and temperature 25 °C. The solid line represents the fit based on the high-RH domain, which coincides with the region of the rapid impedance decline illustrated in Fig. 3. The slope of that linear fit and its interception with abscissa provide estimates of the Weibull shape (κ) and scale (χ) parameters, respectively.

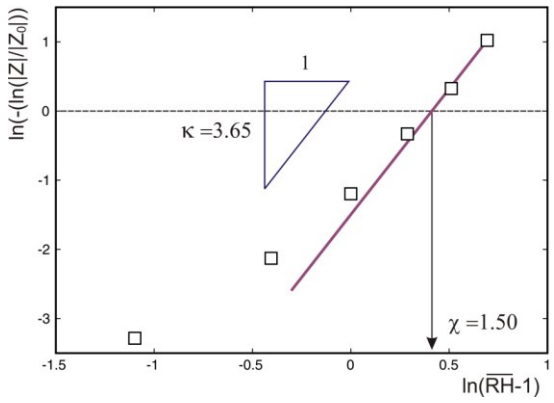

Fig. 6 Estimation of the Weibull parameters (κ, χ) governing the impedance RH sensitivity using the Weibull plot.

These initial estimates of the Weibull parameters with regards to the RH sensitivity of the impedance are included in Table I for various (T, ν) combinations. The values in Table I suggest a trend of increase of κ and χ with increasing frequency at 25 °C, which is not pronounced on elevated temperatures. It cannot be overemphasized that these initial estimates are taken into account when the final (κ, χ) pairs are estimated based on the fitting of the change of impedance with frequency experimental curves (e.g., Fig. 2). These approximated values, presented in the bottom row of Table I, are quite close to the average values, but not necessarily identical to them since they are obtained independently by fine-tuning of the $|Z| = f(\nu|\, RH)$ plots at each temperature.

TABLE I. ESTIMATED VALUES OF WEIBULL PARAMETERS OF SCALE (χ) AND SHAPE (κ) FOR VARIOUS FREQUENCY LEVELS (ROUNDED TO 0.05)

	Temperature [K]					
	298		**323**		**348**	
ν [Hz]	κ	χ	κ	χ	κ	χ
42	3.65	1.5	3.9	1.9	2.9	1.85
100	3.9	1.55	3.8	1.8	2.8	1.85
500	4.0	1.65	4.0	1.95	2.5	1.9
1000	4.1	1.75	4.6	2.1	2.6	2.1
approx.	**3.85**	**1.55**	**4.2**	**1.8**	**2.8**	**1.9**

Finally, Fig. 7 illustrates the resulting mathematical representation of the RH-dependence of the impedance (log $|Z|$) at two frequencies (42 Hz and 500 Hz) and three temperatures (25, 50 and 75 °C). (The base-10 logarithm is selected in this plot for consistency with the experimental data presentation in Fig. 3 and to emphasize more clearly the sudden impedance reduction).

The data fits represented by solid lines correspond to the approximated values of the Weibull parameters presented in Table I, which ignore the abovementioned frequency sensitivity. The fits at $\nu = 42$ Hz (as well as those at $\nu = 100$ Hz omitted herein for brevity) are very good. On the other hand, the fits corresponding to $\nu = 500$ Hz diverge somewhat (less than 5%) from the experimental results at the higher RH levels. This discrepancy (that increases with the temperature decrease) is perhaps not very large but the trend continues at $\nu = 1000$ Hz. This indicates that the simplification of the frequency-insensitivity of (κ, χ) pairs is increasingly iffy at the kHz-level frequencies that correspond to the impedance asymptotic approach to zero.

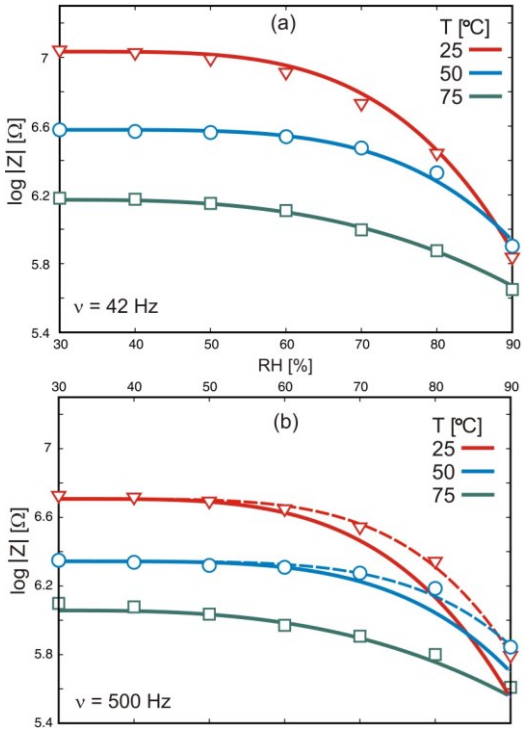

Fig 7 Mathematical representation of the impedance log|Z| change with RH, at frequencies (ν) of 42 Hz and 500 Hz and temperatures of 25, 50 and 75 °C. The solid lines represent fits with approximated (κ, χ) values from Table I while the dashed curves are obtained for (κ, χ) = (4.5, 1.7) and (4.5, 1.95) for 42 Hz and 500 Hz, respectively.

Consequently, it seems that it should be decided on case-by-case basis whether it is worthwhile to include (κ, χ) frequency dependence in the model to account for the high-frequency response distinguished by the low impedance levels of secondary practical importance.

C. Frequency sensitivity

The empirical model (1) accounts for the frequency sensitivity of the impedance using the Weibull function of the same type (4) used for the RH-effect modeling. Naturally, in the case of frequency, the independent variable is the logarithm of the normalized frequency, ln (ν/ν_R), and the corresponding Weibull parameters of scale and shape introduced, respectively, in Eq. (1) as $A = \eta$ and $B = \beta$, respectively. Consequently, the Weibull parameters can be estimated again by using the logarithmic expression (5) and corresponding Weibull plots (similar to Fig. 6). Notably, such plots indicate a change of the Weibull parameters (β, η) at kHz-level frequencies, already observed for (κ, χ). Importantly, this high-frequency response is inherently characterized by fairly negligible impedance levels.

Alternatively, the frequency sensitivity segment of the model (1)

$$\frac{|Z|}{|Z_0|} = \exp\left\{-\left(\frac{x}{\eta}\right)^{\beta}\right\} = F(x|\,\beta,\eta) \tag{6}$$

can be explored by the slope approach outlined in [16] and illustrated by Fig. 8. In Eq. (6), the independent variable $x = \ln(\nu/\nu_R)$ and the dependent variable is the impedance normalized by its maximum value at the particular ambient temperature and RH = 30% (see the left ordinate of Fig. 8).

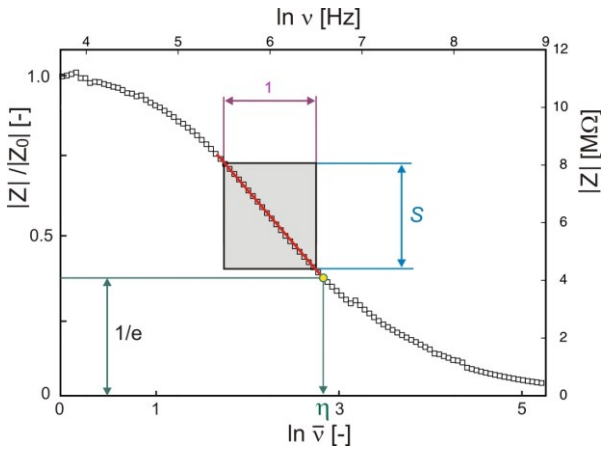

Fig. 8 Geometric interpretation of the Weibull parameter estimation with regards to the frequency (ν) sensitivity of the impedance (|*Z*|) at RH=30% and fixed ambient temperature. The reference values used are $|Z_0|=|Z_R| = 11.$ MΩ and $\nu_R = 42$ Hz.

The maximum slope of the function (6), corresponding to the inflection point, can be derived in the form

$$S \equiv \left.\frac{dF(x)}{dx}\right|_{x=x_\Pi} = \frac{1}{\eta}\,\Xi(\beta) \tag{7}$$

where the shape function

$$\Xi(\beta) = \beta\left(1-\frac{1}{\beta}\right)^{\left(1-\frac{1}{\beta}\right)} \exp\left\{-\left(1-\frac{1}{\beta}\right)\right\} \tag{8}$$

is defined by the Weibull shape parameter β. (The shape function symbol, Ξ, should not be confused with impedance *Z*.) A detailed derivation, which results in Eqs. (7) and (8) is available in reference [16].

As illustrated in Fig. 8, the slope *S* and the Weibull scale parameter η are determined readily from the corresponding experimental plot. Once these parameters (η, *S*) are known, the value of the shape function Ξ can be calculated based on Eq. (7), which enables determination of the Weibull shape parameter β by virtue of Eq. (8).

The pair of Weibull parameters (β, η) governing the impedance frequency sensitivity within the framework of the empirical model (1) are determined for three ambient temperatures used in experiments. As in the previous cases of the temperature-sensitivity and RH-sensitivity parameters, the estimated (β, η) are used as the initial values for the fine tuning of the model output with respect to the experimental results related to the change of impedance (|*Z*|) with frequency (ν) for various RH in the range 30-90% and the fixed ambient temperature (e.g., Fig. 2).

The results related to the model parameter values shown in Table II are shown in Fig. 9. The satisfactory agreement with the experimental results suggests that the Weibull parameters (β, η) are not significantly RH sensitive. Also, the inclined straight dashed line (in a semi-logarithmic plot) indicates that the threshold (onset) of the impedance decrease (marked by empty circles on the curves), at the higher RH levels (70%, 80%, 90%), increases exponentially with increasing RH.

It is significant to note that the bottom row of Table II presents the values of the model parameters that are estimated (based on the values at $T = 25$, 50, 75 °C obtained by fitting the experimental results in the manner just described) for the purpose of the numerical example in the next section. Table II reveals that the power-law exponent τ is rather temperature insensitive. Other parameters, with exception of κ, show a clear tendency to increase with increasing temperature.

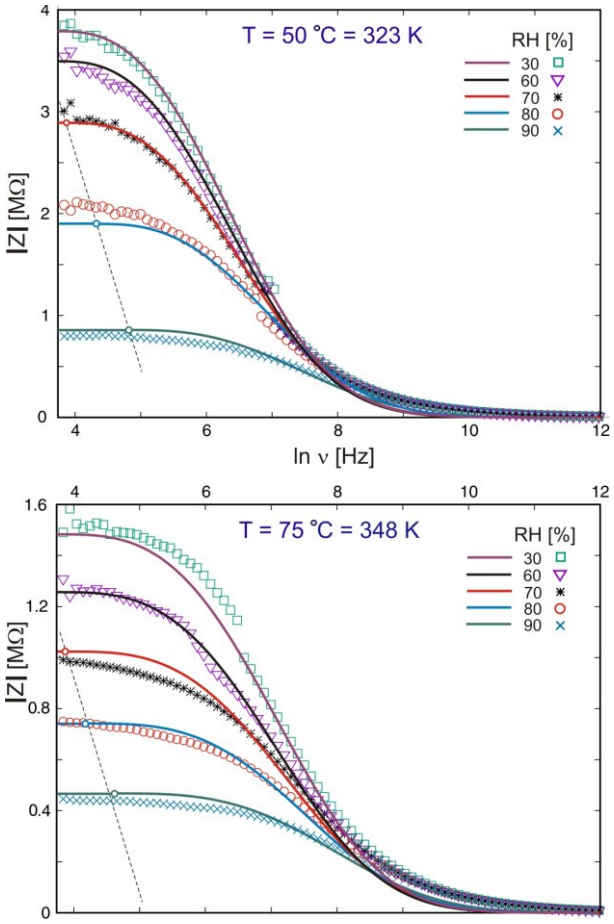

Fig 9 Illustration of the impedance |*Z*| as a function of logarithm of the normalized frequency ($\ln\nu$) for selected RH levels and two ambient temperatures. Discrete symbols mark the experimental data and solid curves the model Eq. (1) results with parameters presented in Table II.

TABLE II. ESTIMATED VALUES FOR WEIBULL PARAMETERS OF SCALE (η, χ) AND SHAPE (β, κ) AND THE TEMPERATURE EXPONENT (τ)

Temperature (K)	Parameters				
	η	χ	β	κ	τ
348	3.8	1.9	3.1	2.8	12.8
323	3.1	1.8	2.7	4.2	13.0
298	2.85	1.55	2.0	3.85	13.0
283	**2.8**	**1.45**	**1.7**	**3.4**	**13.0**

IV. NUMERICAL EXAMPLE

The novel empirical model (1) is now used to predict the change of impedance |*Z*| as a function of RH and frequency at temperature 10 °C, which is outside of the experimentally used temperature range [25, 75] °C. The model parameters used for that purpose are shown in the bottom row of Table II (bold font). As already noted, these estimates are based on the trends among corresponding parameter values illustrated in Table II for the three experimental data sets.

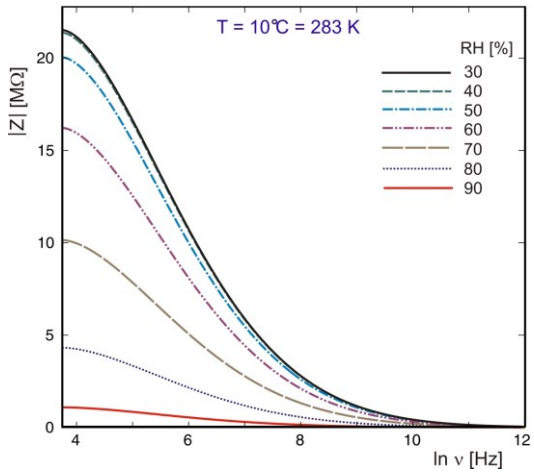

Fig 10 Model prediction of the impedance (|*Z*|) change with frequency (lnν) for ambient temperature 10 °C at various RH levels.

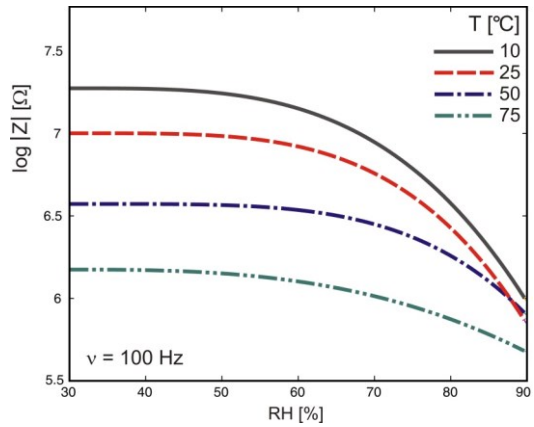

Fig. 11 Model prediction of the impedance (|*Z*|) change with RH for temperatures 10, 25, 50 and 75 °C at frequency 100 Hz. The solid lines represent model output for parameter values presented in Table II.

The model prediction of the change of impedance with frequency in the RH range 30–90 % at 10 °C is illustrated in Fig. 10. Since there are no experimental data to enable a quantitative comparison, one can only emphasize a good qualitative agreement with the experimentally observed *trends* and an increase in the maximum impedance (roughly two times compared to 25 °C), which is in line with our intuitive expectations.

Similarly, the model prediction of the impedance change with RH at frequency 100 Hz and temperatures 10, 25, 50 and 75 °C are presented in Fig. 11. The model prediction in Fig. 11 suggest that the RH threshold associated with the rapid impedance drop decreases by more than 10% as the ambient temperature increases from 10 °C to 75 °C.

V. Summary

Our in-house experimental data sets are used as guidance to develop an empirical model to address the effects of ambient temperature, relative humidity and frequency on impedance change. The proposed mathematical representation is a combination of a reverse-sigmoid function inspired by the three-parameter Weibull cumulative distribution (modeling the relative humidity and frequency sensitivity) and a power law (modeling the temperature sensitivity). The model predictions follow the experimental evidence. In particular, the model reproduces accurately the observed decrease in measured impedance with increase in frequency, RH and temperature. The dynamics of these impedance reductions are captured with reasonable fidelity even for relatively crudely estimated model parameter values that neglect some interdependencies that are perceived to be of secondary importance.

Acknowledgment

This work was financed by the Ministry for Science, Technological Development and Innovations, contract number 451-03-47/2023-1/200053.

References

[1] H. Faharani, R. Wagiran, M. N. Hamidon, “Humidity sensors principle, mechanism and fabrication tehnologies: A Comprehensive Review”, Sensors, vol. 14, pp. 7881-7939, 2014.

[2] Y. Lu, G. Yang, Y. Shen, H. Yang, K. Xu, “Multifunctional flexible humidity sensor systems towards noncontact wearable electronics” Nano-Micro Lett., vol. 14, pp. 150, 2022.

[3] M. V. Nikolic, V. Milovanovic, Z. Z. Vasiljevic, Z. Stamenkovic, “Semiconductor gas sensors: materials, technology, design and application”, Sensors, vol. 20, pp. 6694, 2020.

[4] J. M. Tulliani, B. Inserra, D. Ziegler, “Carbon-based materials for humidity sensing: a short review”, Micromachines, vol. 10, pp. 232, 2019.

[5] M. V. Nikolic, **“**An overview of oxide materials for gas sensors”, 23rd International Symposium on Design and Diagnostics of Electronic Circuits and Systems (DDECS) 20-24 April, 2020, Novi Sad, Serbia.

[6] J. Wang, M. Y. Su, J. Q. Qi, L. Q. Chang, “Sensitivity and complex impedance of nanometer zirconia thick film humidity sensors”, Sens. Actuators B vol. 139, pp. 418-424, 2009.

[7] Z. Wu, J. Yang, X. Sun, Y. Wu, L. Wang, G. Meng et al, “An excellent impedance type humidity sensor based on halide perovskite $CsPbBr_3$ nanoparticles for human respiration modeling”, Sens. Actuators B, vol. 337, pp. 129772, June 2021.

[8] M. V. Nikolic, D. L. Sekulic, Z. Z. Vasiljevic, M. D. Lukovic, V. B. Pavlovic, O. S. Aleksic, “Dielectric properties, complex impedance and electrical conductivity of Fe_2TiO_5 nanopowder compacts and bulk samples at elevated temperatures”, J. Mater. Sci.: Mater. Electron. vol. 28, pp. 4796-4806, 2017.

[9] M. V. Nikolic, J. B. Krstic, N. J. Labus, M. D. Lukovic, M. P. Dojcinovic, M. Radovanovic, N. B. Tadic, “Structural, morphological and textural properties of iron manganite ($FeMnO_3$) thick films applied for humidity sensing”, Mater. Sci. Eng. B, vol. 257, pp. 114547, 2020.

[10] M. V. Nikolic, M. D. Lukovic, M. Dojcinovic, Z. Z. Vasiljevic, N. J. Labus “Application of iron manganite thick films for humidity sensing”, 42nd International Spring Seminar on Electronics Technology (ISSE) 15-19 May 2019, Wroclaw, Poland.

[11] S. Mastilovic, “Some Sigmoid and Reverse-Sigmoid Response Patterns Emerging from High-Power Loading of Solids”, Theor. Appl. Mech., vol. 45, pp. 95-119, 2018.

[12] D. N. Prabhakar Murthy, M. Bulmer, J. A. Eccleston, “Weibull model selection for reliability modeling”, Reliab. Eng. Syst. Saf., vol. 86, pp. 257-267, 2004.

[13] H. Yu, S. H. Zhao, A. S. Mujumdar, X. M. Fang, Z. J. Gao, Z. A. Zheng, H. W. Xiao, “Energy efficient improvements in hot air drying by controlling relative humidity based on Webull and Bi-Di models”, Food Bioproc. Tech., vo. 111, pp. 20-29, 2018.

[14] V. Gburcik, S. Mastilovic, Z. Vucinic, “Assessment of solar and wind energy resources in Serbia”, J. Renew. Sustain. Ener., vol. 5, pp. 041822, 2013.

[15] D. F. Smith, I. M. Hildebrandt, K. E. Casulli, K. D. Dolan, B. P. Marks, “Modeling the effect of temperature and water activity on the thermal resistance of *Salmonella* Enteridis PT 30 in wheat flour”, J. Food. Prot. Vol. 79, pp. 2058-2065, 2016.

[16] S. Mastilovic, B. Djordjevic, A. Sedmak, “A scaling approach to size effect modeling of J_c CDF for 20MnMoNi55 reactor steel in transition temperature region”, Eng. Failure Anal., vol. 131, pp. 105838, 2022.